Deformation, crystal preferred orientations, and seismic anisotropy in the Earth's D " layer

Andrea Tommasi, Alexandra Goryaeva, Philippe Carrez, Patrick Cordier, David Mainprice

Earth and Planetary Science Letters 492 (2018) 35–46

Contents lists available at ScienceDirect

Earth and Planetary Science Letters

www.elsevier.com/locate/epsl

Deformation, crystal preferred orientations, and seismic anisotropy in the Earth's D″ layer

Andréa Tommasi [a,*], Alexandra Goryaeva [b], Philippe Carrez [b], Patrick Cordier [b], David Mainprice [a]

[a] Geosciences Montpellier, CNRS & Université de Montpellier, F-34095 Montpellier cedex 5, France
[b] Univ. Lille, CNRS, INRA, ENSCL, UMR 8207 – UMET – Unité Matériaux et Transformations, F-59000 Lille, France

ARTICLE INFO

Article history:
Received 27 November 2017
Received in revised form 2 March 2018
Accepted 16 March 2018
Available online 10 April 2018
Editor: J. Brodholt

Keywords:
mantle convection
D″ layer
post-perovskite
ferropericlase
deformation modeling
seismic anisotropy

ABSTRACT

We use a forward multiscale model that couples atomistic modeling of intracrystalline plasticity mechanisms (dislocation glide ± twinning) in $MgSiO_3$ post-perovskite (PPv) and periclase (MgO) at lower mantle pressures and temperatures to polycrystal plasticity simulations to predict crystal preferred orientations (CPO) development and seismic anisotropy in D″. We model the CPO evolution in aggregates of 70% PPv and 30% MgO submitted to simple shear, axial shortening, and along corner-flow streamlines, which simulate changes in flow orientation similar to those expected at the transition between a downwelling and flow parallel to the core–mantle boundary (CMB) within D″ or between CMB-parallel flow and upwelling at the borders of the large low shear wave velocity provinces (LLSVP) in the lowermost mantle. Axial shortening results in alignment of PPv [010] axes with the shortening direction. Simple shear produces PPv CPO with a monoclinic symmetry that rapidly rotates towards parallelism between the dominant [100](010) slip system and the macroscopic shear. These predictions differ from $MgSiO_3$ post-perovskite textures formed in diamond-anvil cell experiments, but agree with those obtained in simple shear and compression experiments using $CaIrO_3$ post-perovskite. Development of CPO in PPv and MgO results in seismic anisotropy in D″. For shear parallel to the CMB, at low strain, the inclination of ScS, Sdiff, and SKKS fast polarizations and delay times vary depending on the propagation direction. At moderate and high shear strains, all S-waves are polarized nearly horizontally. Downwelling flow produces Sdiff, ScS, and SKKS fast polarization directions and birefringence that vary gradually as a function of the back-azimuth from nearly parallel to inclined by up to 70° to CMB and from null to ~5%. Change in the flow to shear parallel to the CMB results in dispersion of the CPO, weakening of the anisotropy, and strong azimuthal variation of the S-wave splitting up to 250 km from the corner. Transition from horizontal shear to upwelling also produces weakening of the CPO and complex seismic anisotropy patterns, with dominantly inclined fast ScS and SKKS polarizations, over most of the upwelling path. Models that take into account twinning in PPv explain most observations of seismic anisotropy in D″, but heterogeneity of the flow at scales <1000 km is needed to comply with the seismological evidence for low apparent birefringence in D″.

1. Introduction

The thin shell of the Earth's mantle just above the core, named D″ by Bullen (1949), is an essential feature of the mantle convection system. It forms its lower thermal boundary layer, controlling the thermal, chemical, and mechanical interactions with the core. D″ is expected to be mainly composed of $(Mg,Fe)SiO_3$ (~70%) and (Mg,Fe)O – ferropericlase (Hirose et al., 2015). Experimental results, atomistic modeling, and seismological observations converge to $(Mg,Fe)SiO_3$ being present as bridgmanite, with an orthorhombic perovskite (Pv) structure in hot zones of D″, but acquiring a post-perovskite (PPv) structure in colder regions (cf. review in Hirose et al., 2015).

Seismic velocities in D″ show strong lateral variations at both small and large wavelengths, indicating thermal and chemical heterogeneity (e.g., Lay et al., 1998; van der Hilst et al., 2007). Seismological observations also point to changes in D″ thickness from <100 km to >350 km, which may occur over short lateral distances (e.g., Thomas and Kendall, 2002; van der Hilst et al., 2007). Last but not least, D″ is characterized by spatially

* Corresponding author.
E-mail address: andrea.tommasi@umontpellier.fr (A. Tommasi).

https://doi.org/10.1016/j.epsl.2018.03.032

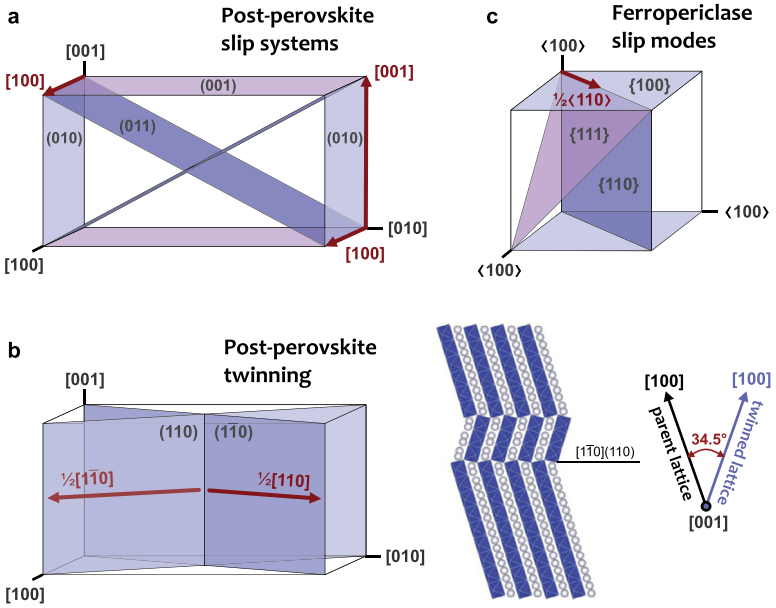

Fig. 1. (a) Slip systems and (b) twinning in $MgSiO_3$ PPv and (c) slip modes in MgO. Note that due to the cubic symmetry of ferropericlase the 3 slip modes displayed in Fig. 1c result in 24 slip systems.

heterogeneous seismic anisotropy, which has been measured using a variety of techniques, such as the analysis of: (i) waveforms anomalies (e.g., Lay and Young, 1991; Maupin, 1994; Cottaar and Romanowicz, 2013), (ii) splitting of shear waves traveling at low incidence angles through D″ (e.g., Kendall and Silver, 1996; Nowacki et al., 2010), (iii) differences between horizontally and vertically polarized shear waves in global tomography models (e.g., Panning and Romanowicz, 2006), (iv) the discrepancy in the residual splitting, after corrections for upper mantle anisotropy, of core shear waves (SKS and SKKS, e.g., Restivo and Helffrich, 2006; Long, 2009), and (v) changes in polarity of P-waves reflected at the top of D″ (e.g., Thomas et al., 2011). These data carry information on the convective flow in D″, but their exploitation depends on our ability to relate the seismic anisotropy observations to deformation-induced compositional layering or crystal preferred orientations of the main rock-forming minerals in D″: bridgmanite, post-perovskite, and ferropericlase. This led to a large number of forward models of development of seismic anisotropy in D″ based on mantle circulation or convection models, which tested different hypotheses on the $(Mg,Fe)SiO_3$ post-perovskite deformation or phase transition mechanisms (e.g., Wenk et al., 2006, 2011; Walker et al., 2011, 2017; Nowacki et al., 2013).

In this article, we also use a forward multi-scale modeling approach for exploring the contribution of deformation-induced crystal preferred orientations (CPO) of PPv and ferropericlase to seismic anisotropy in the D″ layer. We couple the most recent atomistic models of intracrystalline viscoplastic deformation in $MgSiO_3$ PPv and MgO (the pure Mg end-member of both solid solutions) at D″ conditions (Amodeo et al., 2011; Cordier et al., 2012; Goryaeva et al., 2015a, 2015b, 2016, 2017; Carrez et al., 2017) to polycrystal plasticity simulations of simple, end-member flow patterns. Potential effects of this CPO-induced anisotropy on P- and S-waves reflected at the top of D″ are analyzed in a companion article (Pisconti et al., in preparation).

2. Viscoplastic deformation of PPv and MgO at D″ conditions

Numerical modeling of the dislocation structures and glide properties in $MgSiO_3$ PPv and MgO at lowermost mantle strain rates, temperatures, and pressures (Amodeo et al., 2011; Cordier et al., 2012; Goryaeva et al., 2015b, 2016, 2017) constrain the active slip systems in the two minerals and their relative strengths under D″ conditions (Fig. 1 and Table 1). These models predict that the easiest slip systems for both minerals, namely $[100](010)_{PPv}$ and $[001](010)_{PPv}$ and $1/2\ \langle 110\rangle\{1\bar{1}0\}_{MgO}$ and $1/2\ \langle 110\rangle\{100\}_{MgO}$, have extremely low lattice frictions under lowermost mantle conditions, implying low strengths for mantle flow by dislocation creep in domains with high volume fractions of PPV in D″. In contrast, similar models for bridgmanite predict extremely high lattice frictions for all studied slip systems, implying that dislocation glide is not an effective deformation process for this phase in the lower mantle (Kraych et al., 2016). Dislocation dynamics models predict that bridgmanite should rather deform by pure climb (Boioli et al., 2017) and, hence, not develop strong CPO under lower mantle conditions. The corollary of these models is that PPv-rich domains in D″ should develop strong CPO of both PPv and ferropericlase, leading to a marked anisotropy of physical properties, whereas bridgmanite-rich ones should have much lower anisotropies, only controlled by the CPO of ferropericlase.

In PPv, if only dislocation glide is active, no strain parallel to the [100], [010], or [001] crystal axes can be accommodated. However, atomic-scale models for PPv also predict the development of $1/2\ \langle 110\rangle\{1\bar{1}0\}$ deformation twins (Carrez et al., 2017). {110} twinning should play a significant role in the evolution of the CPO in PPv, since it adds additional degrees of freedom for deformation (it may accommodate strain parallel to [100] and [010]), reducing strain incompatibility problems.

3. Modeling strain-induced CPO evolution and associated seismic anisotropy in D″

Development of CPO in PPv and MgO polycrystals deformed under D″ conditions is modeled by a viscoplastic self-consistent (VPSC) approach (Molinari et al., 1987; Lebensohn and Tomé, 1993), which considers each grain as a viscoplastic inclusion embedded in and interacting with a viscoplastic effective medium that represents the average behavior of the polycrystal. Each grain deforms by dislocation glide only (MgO) or by dislocation glide and twinning (PPv); these processes allow for shear in a finite set of crystallographic planes and directions (Fig. 1). Diffusive processes are only implemented in an implicit way. First, by assuming that they contribute to recovery mechanisms, such as climb, which

Table 1
Slip systems and twinning data used in the different simulations. Critical Resolved Shear Stresses (CRSS) for the different systems were derived based on atomic scale models of intracrystalline deformation in $MgSiO_3$ post-perovskite and MgO (a full description of the procedure is presented in the online supplementary material).

Slip/twinning systems' CRSS		Model			
		Reference model: Twin-1	NoTwin-1	Twin-2	NoTwin-2
$MgSiO_3$ PPV	[100](010)	**1**	1	1	1
	[001](010)	**1**	1	3	3
	[100]{011}	**10**	10	10	10
	[100](001)	**20**	20	20	20
	1/2 ⟨110⟩{1$\bar{1}$0}	**3**	–	3	–
	⟨110⟩{111}[a]	**50**	50	50	50
	⟨011⟩{111}[a]				
MgO	1/2 ⟨110⟩{1$\bar{1}$0}	**1**	1	1	1
	1/2 ⟨110⟩{100}	**1**	1	1	1
	1/2 ⟨110⟩{111}	**5**	5	5	5

[a] Mark auxiliary systems (not predicted by atomistic models), which are included in the calculations for numerical stability; their high CRSS ensure that they never accommodate >2% of the aggregate strain. Differences in CPO evolution between models Twin-1 (NoTwin-1) and Twin-2 (NoTwin-2) are only significant at shear strains higher than 5. The comparison of the CPO intensity evolution in the four models is shown in Fig. 4; full CPO patterns for model Twin-2 are presented in the online supplementary material.

avoid hardening but do not produce strain in the present models. Second, by assuming that they contribute to accommodate the strain components that cannot be produced by the known slip systems or twinning in PPv, which in the models are accommodated by "auxiliary slip systems", not predicted by atomic-scale models but imposed to close the yield surface of the PPv crystal.

CPO evolution is controlled by the imposed deformation, the initial texture, and the active slip and twinning systems, which depend on the mineral structure, but also on the temperature and pressure conditions, which control their relative strength or critical resolved shear strength (CRSS). Here, we use CRSS derived from the atomic scale models of dislocation structures and glide properties in PPv and MgO at D″ strain rates, temperatures, and pressures discussed in the previous section (Table 1; the full description of the procedure used for establishing the different CRSS sets tested in the present study is presented in the online supplementary material). High CRSS (50, Table 1) are imposed to the "auxiliary slip systems" in PPv. This ensures that they never accommodate more than 2% of the total viscoplastic strain and do not significantly affect the CPO evolution.

Actual stress-strain rate relations for PPv are not known. However, recent dislocation dynamics simulations for MgO suggest a typical dislocation creep regime in D″ (Reali et al., 2017). In this regime, most of the deformation is accommodated by dislocation glide, but strain rates are controlled by recovery by climb, leading to a steady state behavior described by a power law with stress exponent (n) values around 3. Given the high temperatures considered in the present simulations, we suppose that PPv has a similar behavior. Thus simulations for both PPv and MgO were run with $n = 3$ for all slip and twinning systems and no hardening.

Twinning in PPv is modeled using the Predominant Twin Reorientation Scheme proposed by Tomé et al. (1991). Similarly to dislocation glide, twinning is described as a shear deformation on a given plane and direction (for PPv, 1/2 ⟨110⟩{1$\bar{1}$0}, Fig. 1b). Its activation is controlled by a CRSS (Table 1). Twinning differs nevertheless from slip by its unique sense of shear, which is modeled by activating twinning only if the resolved shear stress has the same sign as the slip direction. The total crystal viscoplastic strain is the sum of the shear on all slip and twin systems. The effect of twinning on the CPO evolution is modeled in a statistical way by changing the orientation of the entire crystal when the twinned volume in the grain is higher than a threshold (50% in the present models). Different values for the parameters controlling the evolution of the twinned volume in the grain were tested; the results are presented in the online supplementary material. Hardening associated with the formation of twins is neglected, because the models are set for high temperatures. We also run models in which twinning was suppressed (NoTwin-1 and NoTwin-2 models, Table 1).

We first investigate the evolution of CPO in aggregates of 1000 crystals with a random initial preferred orientation composed of 70% PPv and 30% MgO submitted to two end-member deformation regimes: axial shortening (for comparison with experimental data) and simple shear. Simple shear models were run up to a shear strain of 10; this would correspond to a horizontal displacement of 2500 km in a 250 km thick D″ layer if the strain was homogeneously distributed. Actual flow in D″ is most likely three-dimensional, but regions submitted to large deformations probably display a strong shear component, whose orientation relatively to the CMB will depend on the large-scale convection pattern. Changes in CPO evolution in transpression and transtension relative to simple shear are analyzed in the online supplementary material. Finally, we modeled the CPO evolution along two 2D corner-flow streamlines in an isoviscous Newtonian fluid (Batchelor, 1967). These streamlines are not representative of any actual flow in D″, but allow studying the effect of changes in flow direction, such as those expected at the transition between a downwelling slab and flow parallel to the CMB within D″ or between shear parallel to the CMB and upwelling at the borders of a LLSVP, on CPO patterns and seismic anisotropy in D″. The velocity gradients along the modeled streamlines are presented in the online supplementary material (Table S1); the associated strain rates are $\sim 10^{-15}$ s^{-1}.

To test for the effect of the linearization scheme, tangent and second order VPSC models (Lebensohn and Tomé, 1993; Lebensohn et al., 2005) were run. The effect of changing the linearization scheme is found to be minor. The CPO patterns are similar, although the CPO evolves slightly slower in second order models. Thus we present only the more accurate second order VPSC models.

Seismic properties for 70% PPv – 30% ferropericlase aggregates were calculated using the modeled CPOs and elastic constant data of Wu et al. (2013) for ferropericlase and Zhang et al. (2016) for PPv using the MTEX Matlab toolbox (Mainprice et al., 2011). The calculations were performed for compositions of $(Mg_{0.75}Fe_{0.25})SiO_3$ and $(Mg_{0.8125}Fe_{0.1875})O$, temperatures of 2000 K, and pressures of 125 GPa. It is important to note that changes in Fe and Al contents in PPv, as well as in pressure and

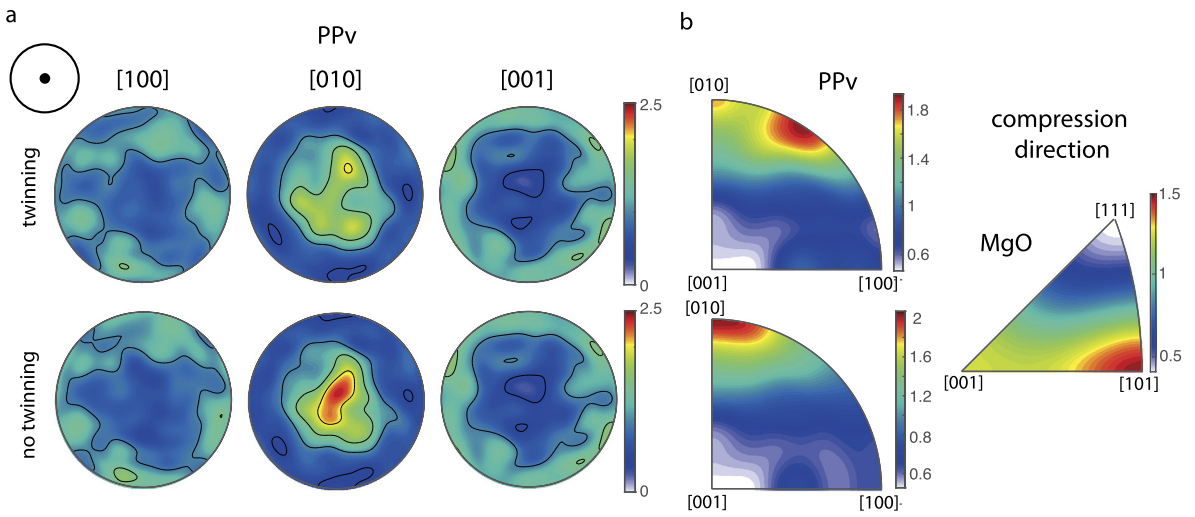

Fig. 2. PPv and MgO CPO after 20% of axial shortening for models in which twinning is active (top) or suppressed (bottom). (a) Pole figures of the PPv CPO; stereographic projections, contours at 0.5 multiples of uniform distribution (m.u.d). (b) Inverse pole figure (IPF) of the shortening direction for PPv and MgO (similar for the two models). Insert on the top left indicates the reference frame of the pole figures, with the black circle marking the shortening direction. (For interpretation of the colors in the figure(s), the reader is referred to the web version of this article.)

temperature in the ranges expected to occur in D″ produce minor variations of the anisotropy patterns and intensity (Zhang et al., 2016 and online supplementary Fig. S3), which do not change the conclusions of the present study.

4. Results

4.1. CPO evolution in axial compression

Axial compression produces a fiber-[010] PPv CPO characterized by a maximum of $[010]_{PPv}$ at low angle to the compression direction (black dot in the center of pole figure) and girdles of $[100]_{PPv}$ and $[001]_{PPv}$ at high angle to it (Fig. 2). This CPO, although weak, is already well developed at 20% shortening. Suppression of twinning leads to stronger alignment of $[010]_{PPv}$ with the shortening direction and faster concentration of the CPO as a function of strain.

MgO also develops an axisymmetric CPO characterized by alignment of $[101]_{MgO}$ parallel to the compression direction (Fig. 2). With increasing strain, the PPv CPO becomes stronger, but the pattern remains constant. In contrast, MgO develops a strong alignment of $[001]_{MgO}$ parallel to the compression direction in addition to the initial $[101]_{MgO}$ maximum, which becomes a secondary orientation component.

4.2. CPO evolution and development of seismic anisotropy in simple shear

Simple shear results in development of a monoclinic PPv CPO, which progressively rotates towards parallelism between the dominant $[100](010)_{PPv}$ slip system and the macroscopic shear (Fig. 3). The $[010]_{PPv}$ axis displays the strongest concentration, which tends, for shear strains greater than 2, to align normal to the shear plane. $[100]_{PPv}$ and $[001]_{PPv}$ axes form girdles at low angle to the shear plane, with a weak $[100]_{PPv}$ maximum aligned with the shear direction and, at high strains, a $[001]_{PPv}$ maximum normal to it. Rotation of the twinned fractions by 34.5° around the [001] axis (Fig. 1b) produces dispersion of $[100]_{PPv}$ and of $[010]_{PPv}$ on the XZ plane, that is, in a plane normal to the shear plane but containing the shear direction.

In the present study, PPv and MgO are modeled as having similar viscoplastic strengths (Table 1). By consequence, strain tends to be evenly partitioned between the two phases. However, the high number of available slip systems in MgO (the 3 slip modes listed in Table 1 provide 24 slip systems due to the cubic crystal symmetry) results in weaker CPO relative to PPv (Fig. 3). Maximum concentrations are $\leq$2 multiples of a uniform distribution, even at a shear strain of 10. Both the intensity and CPO patterns of MgO vary in a periodic manner with increasing shear strain, without attaining a stable orientation (as also observed in large strain shearing of halite, which is isostructural with MgO by Wenk et al., 2009). Well-developed MgO CPO are nevertheless characterized by concentration of $\langle 100 \rangle_{MgO}$ normal to the shear plane and a weaker concentration of $\langle 110 \rangle_{MgO}$ parallel to the shear direction.

These PPv and MgO CPO result in marked anisotropy for both P- and S-waves propagating through D″. The PPv CPO controls the seismic anisotropy, but the MgO contribution results in lower maximum P- and S-wave anisotropies than a 100% PPv aggregate with the same CPO. Similarly to the PPv CPO, fast P-waves propagation directions and fast S-waves polarization planes rotate towards parallelism with the shear direction with increasing shear strain (Fig. 3). Both P- and S-waves maximum propagation and polarization anisotropies increase non-linearly with increasing strain: quickly up to shear strains of 2, slower thereafter (Fig. 4).

P-wave propagation anisotropy patterns have an orthorhombic symmetry (Fig. 3). At low strains, the highest P-wave velocity corresponds to propagation parallel to the lineation (maximum elongation direction), which is at ~20° anticlockwise to the shear direction, and the lowest, to propagation along the maximum shortening direction. With increasing strain, the pattern evolves towards transverse isotropy with a slow symmetry axis normal to the shear plane and high P-wave velocities for most propagation directions in the shear plane.

Shear wave polarization anisotropy patterns also change with increasing strain (Fig. 3). At a shear strain of 1, high birefringence is observed in the foliation plane (plane normal to the maximum finite shortening direction), which is at ~20° anticlockwise to the shear plane, with a 90° periodicity: the highest birefringence is observed for S-waves propagating parallel or normal to the lineation (maximum finite elongation direction). Weak birefringence is predicted for S-waves propagating in the XZ plane at $\geq$30° to the lineation. At shear strain of 2, significant birefringence ($\geq$2.5%) is predicted for all propagation directions at high angle to the shear direction, with the highest anisotropy (4.7%) for S-waves propagating normal to the shear direction in the shear plane. Apparent isotropy is predicted for S-waves propagating in the XZ plane obliquely to the shear direction. At shear strains $\geq$5, most S-waves propagating obliquely to the shear plane sample high birefringence ($\geq$3%).

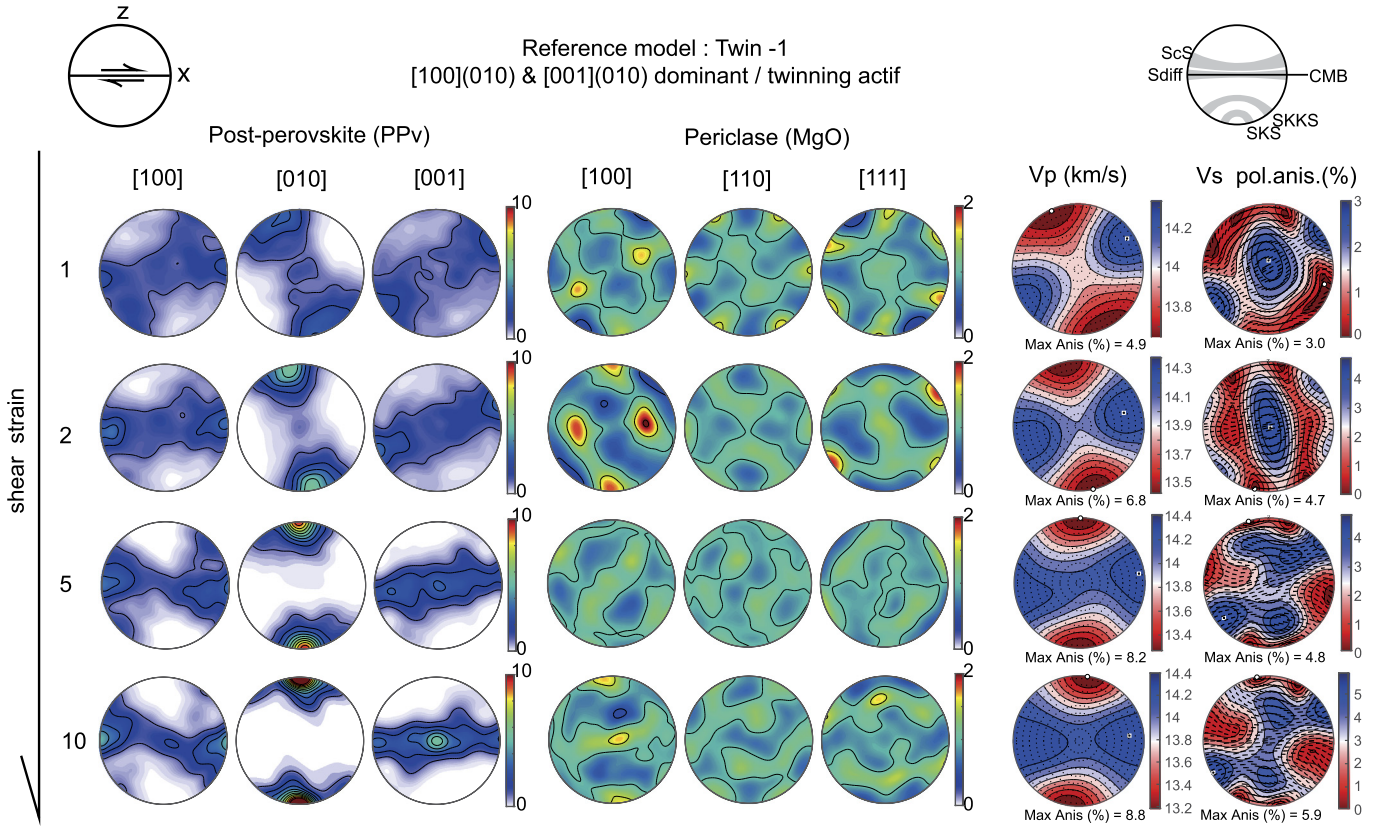

Fig. 3. Evolution of PPv and MgO crystal preferred orientations and seismic anisotropy with increasing shear strain for the reference model (Twin-1). Lower hemisphere stereographic projections. Contours at 1 multiple of uniform distribution (m.u.d) for PPv and at 0.2 m.u.d for MgO. Insert on the top left shows the structural reference frame and the one in the top right, the directions sampled by different S-waves traveling in D″ if the shear plane is parallel to the CMB.

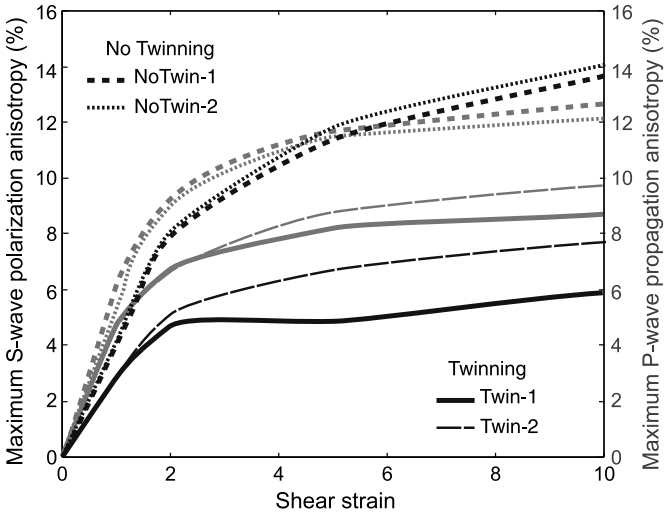

Fig. 4. Evolution of the maximum P-wave propagation (gray) and S-wave polarization anisotropy (black) with increasing shear strain for models with and without twinning. CRSS values for the different models are presented in Table 1.

Fig. 5 displays the birefringence of S-waves with different incidence angles in D″ predicted for shearing parallel to the CMB based on the models shown in Fig. 3. At low shear strains, all S-waves show a strong variability of both the direction of fast-polarization (in Fig. 5 is displayed the inclination of the fast polarization direction relatively to the horizontal, which is what can be measured seismologically, cf. Fig. 6 in Wookey and Kendall, 2008) and of the intensity of the birefringence as a function of the propagation direction. Sdiff waves display strong birefringence for fast-polarizations inclined by 25–50° to the horizontal and lower birefringence for subhorizontal fast polarizations. ScS and SKKS waves show a strong variation of the orientation of fast polarization directions, which range for SKKS from near horizontal to inclined by >50°, as a function of the propagation direction. SKS waves display lower birefringence and lower maximum inclination angles for the fast polarization direction (>30°). With increasing shear strain, the azimuthal variability in the birefringence is preserved or even enhanced, but the maximum inclination angles of the fast polarization directions decrease. Maximum ScS fast-polarization direction inclinations, for instance, are of 25° for a shear strain of 2 and of 15° for a shear strain of 5. Higher inclinations (up to 30°) are observed for shear strains of 10, but they are associated with low birefringence.

Suppression of twinning in PPv (model NoTwin-1, Table 1) results in a CPO with a clear orthorhombic symmetry, which intensity evolves faster than in the reference model (Fig. 6). It also leads to slower rotation of the CPO towards parallelism between the easy [100](010) slip system and the imposed macroscopic shear, which is not fully attained even at a shear strain of 10. For high strains, suppression of twinning results in point distributions for all three axes: [100], [010], and [001], but the latter has a lower concentration. Seismic anisotropy patterns are similar to those in the models with twinning, but anisotropies at any given finite strain are higher (Fig. 4). In addition, seismic anisotropy patterns are slightly oblique to the shear reference frame even at a shear strain of 10, due to the slower rotation of the CPO towards parallelism between the dominant slip system and the macroscopic shear in the models were twinning is suppressed (Fig. 6).

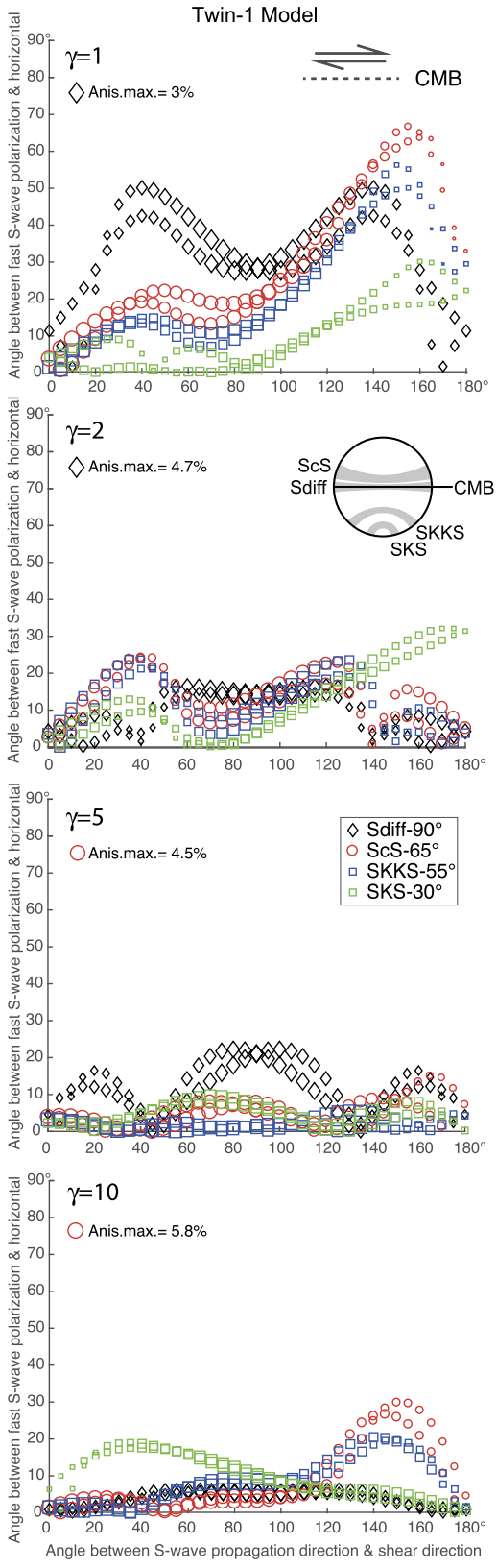

Fig. 5. Birefringence of S-waves with different incidence angles in D″ (cf. insert) as a function of the propagation direction (measured relatively to the shear direction), predicted for the models displayed in Fig. 3 considering that the shear plane is parallel to the CMB (considered locally as horizontal). The birefringence is expressed by both the inclination of the direction of fast-polarization relatively to the horizontal and the intensity of the anisotropy (size of the symbols).

4.3. CPO and seismic anisotropy evolution in response to a change in flow direction

The PPv CPO evolution along a downwelling flow, starting from random orientations at 300 km above the CMB (based on the hypothesis that bridgmanite deforms dominantly by climb and does not develop CPO, Boioli et al., 2017), is characterized by a slow rotation of [100] towards the vertical, which is not completed before the downwelling impacts the CMB and the flow evolves into dominant shearing parallel to the CMB (Fig. 7). At the corner, the change in flow pattern leads to progressive evolution of the CPO towards one better oriented to accommodate the imposed shearing parallel to the CMB. This results, first, in weakening of the CPO (Fig. 7). New maxima of [100] parallel to the flow direction and [010] normal to the shear plane develop and are progressively reinforced, whereas those formed in the downwelling path decrease in intensity. Typical horizontal shearing CPO are observed at >300 km from the downwelling (Fig. 7).

The downwelling path is characterized by predominance of fast S-wave polarizations inclined relatively to the CMB (Fig. 7). The intensity of the anisotropy increases with depth. Both the anisotropy intensity and the inclination angle of the fast polarization vary markedly as a function of propagation direction. At the end of the downwelling path, they range from null to 4.7% and from subhorizontal to >50°, respectively. ScS and Sdiff waves propagating parallel to the "slab" trend sample the highest birefringences, which, at the end of the downwelling path, are associated with fast-polarizations inclined by up to 50° to the horizontal (Fig. 7). Core shear waves (SKS and SKKS) sample weaker birefringences along their paths in D″ in the vicinity of a downwelling. Close to the corner, depending on the back-azimuth, SKKS might nevertheless sample up to 3% of birefringence. For most back-azimuths, SKS sample lower birefringences and show lower inclinations of the fast polarization direction than SKKS (Fig. 7).

The weakening of both PPv and MgO CPO in response to the change in flow direction results in reduction of the anisotropy and rather complex S-wave splitting patterns up to 300 km away from the downwelling (Fig. 7). In this interval, Sdiff, ScS, and SKKS waves display fast polarizations, which change sharply from inclined to parallel to the CMB, and highly variable delay times as a function of the back-azimuth (Fig. 7). ScS and SKKS waves may display fast-polarization directions inclined by >50° from the horizontal. SKS display a lower back-azimuthal variability, with fast polarization directions inclined by ≤30° from the horizontal. Sdiff only show strong birefringence for propagation directions within ±30° of the flow direction and have in this case, subhorizontal fast-polarization directions (Fig. 7).

At >300 km from the downwelling (Fig. 7), fast S-waves polarizations for all incidence angles and propagation directions are dominantly subhorizontal (<20°). Delay times still depend on the propagation direction. Sdiff, ScS, SKKS, and SKS waves propagating at high angle to the flow direction sample high birefringences (>3.5%). For other propagation directions, Sdiff and SKS sample low birefringence (0–2%). In contrast, ScS and SKKS waves propagating in the plane that contains the flow direction sample rather high birefringence (≥3%).

Despite the contrast in initial CPO (the upwelling calculation was initialized with the CPO predicted for a horizontal shear strain of 10 in Fig. 3), the change from shear parallel to the CMB to upwelling, which might occur, for instance, at the boundaries of LLSVPs, also produces weakening of the PPv CPO and of the associated seismic anisotropy in most of the upwelling path in D″ (Fig. 8). Even early in the upwelling path (within <100 km of the corner, Fig. 8), ScS, SKKS, SKS waves show dominantly inclined fast-polarizations. The latter vary as a function of the propagation direction between 30° and 65° for ScS waves and between 40° and

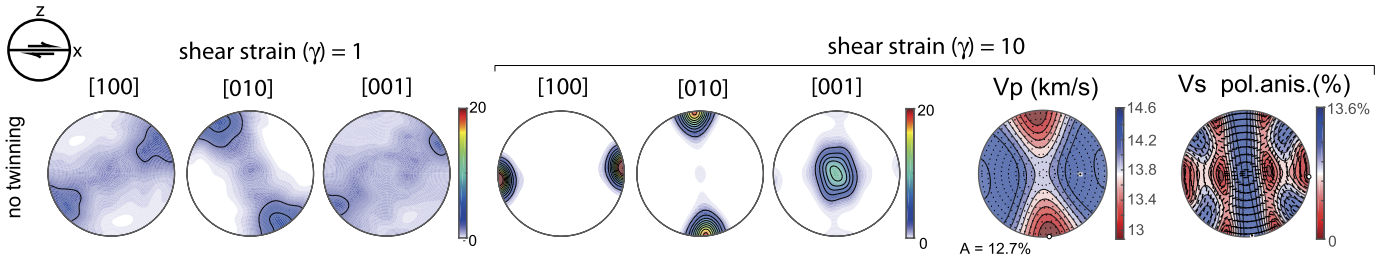

Fig. 6. Evolution of PPv crystal preferred orientations at shear strains of 1 and 10 and seismic anisotropy at a shear strain of 10 for Model NoTwin-1 (twinning suppressed). Lower hemisphere stereographic projections, contours at 2 multiple of uniform distribution (m.u.d). Note that the maximum intensity of the scale bar in the CPO stereoplots is twice the one in Fig. 3. Insert on the top left shows the structural reference frame.

60° for SKKS, with the higher inclinations, but lower birefringence observed for waves propagating in planes that are either at low or high angle to the X-direction (Fig. 8). SKS waves show almost no back-azimuthal variability in the inclination of the fast-polarization direction, which is ∼30°. Sdiff waves, in contrast, display nearly horizontal fast-polarizations and strong birefringence for all propagation directions, except those at high angle to X, which are characterized by inclined fast-polarizations and low birefringence. At >200 km from the corner, a clear vertical shearing CPO develops. It results in strongly inclined (65–90°) fast-polarizations for Sdiff waves and in strong azimuthal variability in the inclination of the fast-polarization for ScS and SKKS waves (from 0° to 65° and from 0° to 50°, respectively). SKS waves show lower maximum inclinations of the fast-polarizations (≤25°). All S-waves show a strong variability of the intensity of the birefringence as a function of the propagation direction (Fig. 8).

Actual flow patterns in D″ are certainly more complex then the two corner flow lines studied here. Geodynamic models show time-dependent flow patterns with frequent buckling of the slabs when impinging upon the CMB (McNamara et al., 2002). Com-

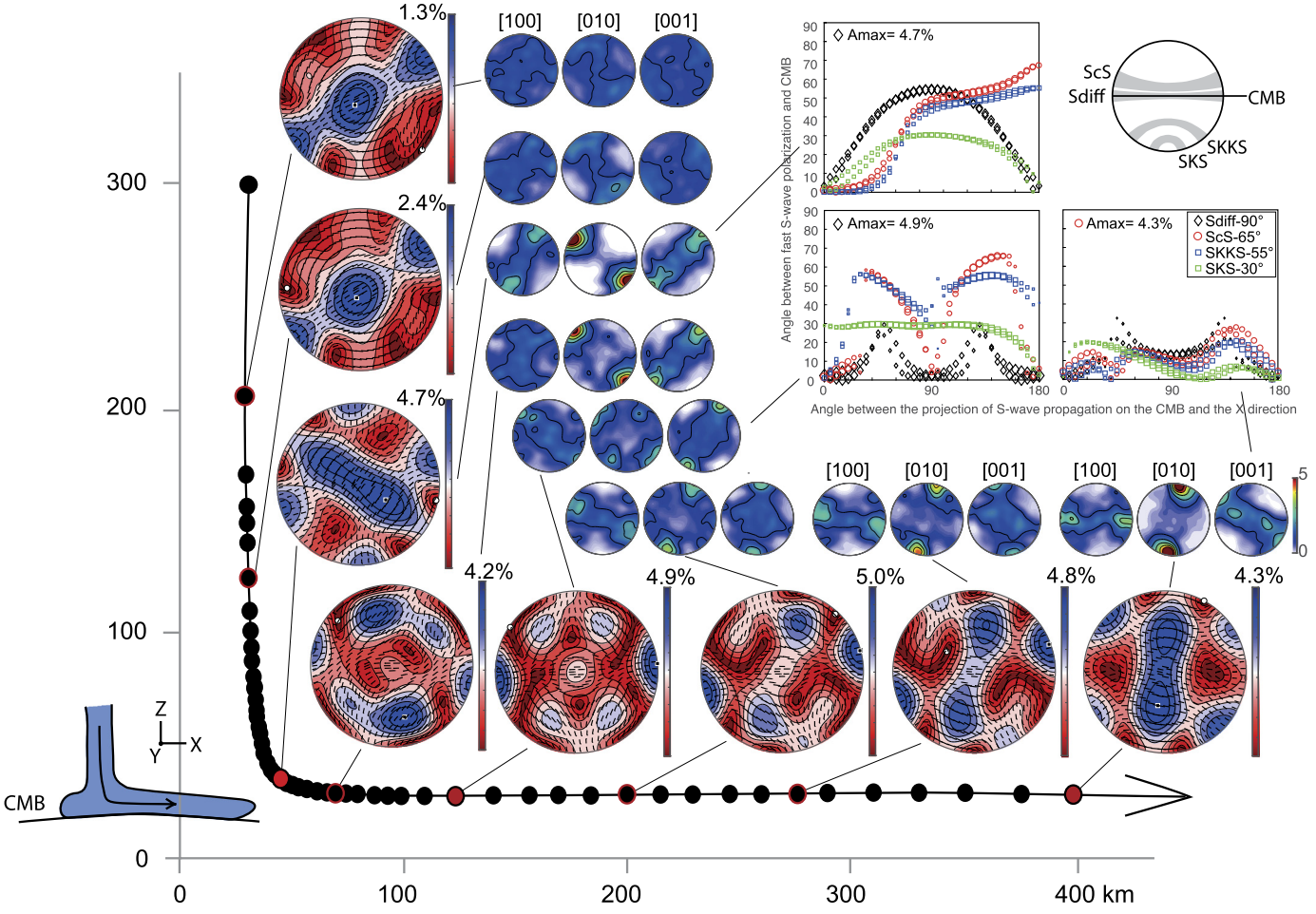

Fig. 7. Evolution of the PPv CPO and of the S-waves polarization anisotropy predicted for the 70% PPv + 30% MgO aggregate along a corner flow line simulating the change in flow direction associated with the transition from a downwelling to shearing parallel to the CMB (cf. sketch at the bottom left of the figure). Lower hemisphere stereographic projections. All CPO pole figures use the same coloring range, between 0 and 5 multiples of a uniform distribution, for easy visualization of the changes in CPO intensity. S-wave polarization anisotropy plots are colored independently from each other, the local maximum birefringence (white square) is indicated at the top right of each pole figure. Plots at the top right show the variation of the angle between the fast polarization direction and the horizontal (equated locally to the CMB) as a function of the propagation direction measured relatively to X for S-waves that sample D″ with different incidence angles (cf. insert at top right) at 3 selected locations along the flow line (red dots). CPO calculations were performed using Twin-1 CRSS set (Table 1). The velocity gradient evolution imposed along the flow line is presented in the Online Supplementary Material.

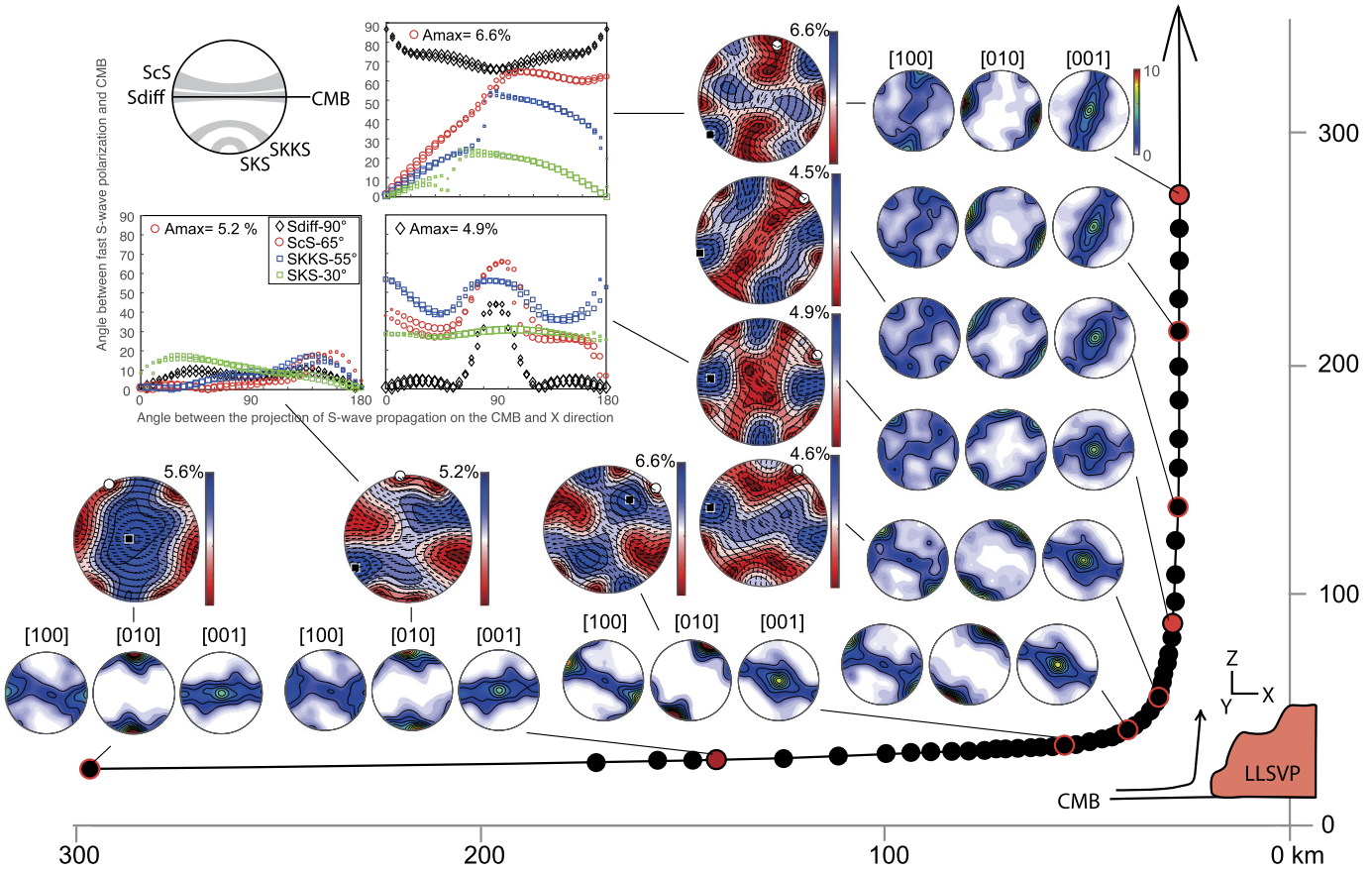

Fig. 8. Evolution of the PPv CPO and of the S-waves polarization anisotropy predicted for the 70% PPv + 30% MgO aggregate along a corner flow line simulating the change in flow direction associated with the transition from shearing parallel to the CMB to upwelling at the border of a LLSVP (cf. sketch at the bottom right of the figure). Lower hemisphere stereographic projections. All CPO pole figures use the same coloring range, between 0 and 10 multiples of a uniform distribution, for easy visualization of the changes in CPO intensity. S-wave polarization anisotropy plots are colored independently from each other, the local maximum birefringence (white square) is indicated at the top right of each pole figure. Plots at the top left show the variation of the angle between the fast polarization direction and the CMB as a function of the propagation direction measured relatively to X for S-waves that sample D″ with different incidence angles (cf. insert at top left) at 3 selected locations along the flow line (red dots). CPO calculations were performed using Twin-1 CRSS set (Table 1). The velocity gradient evolution imposed along the flow line is presented in the Online Supplementary Material.

positionally stratified slabs may also rotate, so that the denser crustal layer faces down (Tackley, 2011). In addition, plumes may form at the edges and sides of the slabs, disrupting the horizontal slab spreading atop the CMB (Tackley, 2011). The present models give, nevertheless, a first order understanding on how the CPO evolution and seismic anisotropy will respond to such changes in flow patterns: CPO and seismic anisotropy patterns do reorient in response to the changing flow field, but with a delay, which may correspond spatially to up to 300 km for an average strain rate of 10^{-15} s^{-1}, which is the one used in the present models. Faster strain rates will result in faster strain accumulation and hence in faster reorientation of the CPO and seismic anisotropy patterns; the opposite is also true. In most cases, as those modeled here, sharp changes in flow direction result in local weakening of the CPO and, hence, limit the strengthening of the anisotropy. Yet, this weakening may not occur if the preexisting CPO is well oriented to accommodate the new deformation field.

5. Discussion

5.1. Comparison to experimental data on PPv deformation

Experimental data on CPO development in PPv comprise moderate temperature and pressure compression and simple shear experiments on $CaIrO_3$ PPv (Yamazaki et al., 2006; Miyagi et al., 2008; Niwa et al., 2012), which maintains the post-perovskite structure at ambient conditions, allowing therefore post-mortem analysis of the deformation microstructures, and laser-heated diamond-anvil cell (DAC) compression experiments on $MgGeO_3$ and $(Mg,Fe)SiO_3$ PPv. The latter experiments better reproduce actual D″ compositions and pressure and temperature conditions, but they have poorly controlled boundary conditions, involve multiple phase transformations and very high stresses (>GPa), and cannot be quenched.

Despite significant differences in bond strengths and elastic properties between $MgSiO_3$ and $CaIrO_3$ post-perovskites (Metsue et al., 2009), CPO evolutions predicted in the present study are in excellent agreement with those observed in experimental deformation of $CaIrO_3$ PPv in both compression and simple shear (Yamazaki et al., 2006; Miyagi et al., 2008; Niwa et al., 2012). {110} twins were also observed by TEM in deformed $CaIrO_3$ post-perovskite (Niwa et al., 2012).

The modeled CPO (Fig. 2) are nevertheless at odds with CPO developed in laser-heated diamond-anvil cell (DAC) experiments on $(Mg,Fe)SiO_3$ PPv and on $MgGeO_3$ PPV, which are characterized by a concentration of (102), (100), or (001) normal to the compression direction (Merkel et al., 2007; Miyagi et al., 2010; Wu et al., 2017). There is no straightforward explanation for these CPO, which are not supported by our current understanding of the microphysics of viscoplastic deformation in PPv. They might be due to pre-texturing of PPv due to viscoplastic deformation of the precursor phases and inheritance upon phase transition, as proposed to explain (100) and (102) textures (Miyagi et al., 2010), or

to the high differential stresses at play in the experiments, which may allow the activation of slip systems with high CRSS, such as $[100](001)_{PPv}$ (Table 1). The latter behavior has indeed been observed during cold compression of wadsleyite (Thurel and Cordier, 2003).

5.2. Comparison to observations of seismic anisotropy in D″

Seismic measurements of anisotropy in D″ are essentially based on the analysis of the birefringence of S-waves with different incidence angles and paths in D″. Despite the common use of 'transverse isotropic' models with different orientations of the symmetry axis to interpret seismic anisotropy observations in D″, the present models, independently of the choice of input parameters (CRSS of the different slip systems and activation of twinning or not), imply that seismic anisotropy patterns in D″ should have an orthorhombic symmetry, with both radial and azimuthal anisotropy components. The models also show that the S-wave birefringence (orientation of the fast-polarization and intensity of the anisotropy) depends on the orientation of the propagation direction relatively to the flow. For monotonic simple shear or transpression, at shear strains higher than 2, although the intensity of the anisotropy varies as a function of the propagation direction, the polarization of fast S-waves is dominantly at low angle ($>20°$) to the shear direction (Fig. 3 and Supplementary Material Figs. S1 and S2). However, at low shear strains, in transtension, or subsequently to a change in flow direction, fast S-wave polarizations might be highly oblique to the local flow direction (Figs. 3, 5, 7, 8 and Supplementary Material Figs. S1 and S2). The maximum birefringence varies from 3% at a shear strain of 1 to 6% at a shear strain of 10. Increasing pressure and temperature to 3500 K and 150 GPa does not significantly change the above predictions (Online Supplementary Material Fig. S3).

In the next paragraphs, we compare these predictions to observations of seismic anisotropy in D″. These observations depend on multiple corrections to isolate the lowermost mantle signal and may be biased by effects arising from complexity in the lowermost mantle structure or noise (cf. Komatitsch et al., 2010; Monteiller and Chevrot, 2010; Panning et al., 2010; Chang et al., 2014; Borgeaud et al., 2016). These possible biases will be ignored in the following discussion. More importantly, observations of seismic anisotropy in D″ integrate the anisotropic signal not only over long paths, which range from a 300–400 km for SKS and SKKS to 1000–3000 km for ScS and Sdiff, but also, due to finite-frequency effects, over large volumes (banana-doughnut sensitivity kernels) around the path (Favier and Chevrot, 2003; Sieminski et al., 2009). The present models do not allow testing the effect of the integration of a spatially variable anisotropy signal, since we only calculate the CPO and seismic anisotropy evolution in response to a few simple strain histories. However, they allow to discuss which flow patterns may produce the observed seismic anisotropy. In addition, by considering that the different anisotropic contributions (ponderated by the local anisotropic kernel sensitivity) add up if the orientation of the fast polarization is similar or combine in a more complex manner if the orientation of the anisotropy varies, producing in general lower delay times and intermediate orientations of the fast axes (Favier and Chevrot, 2003; Nowacki and Wookey, 2016), we try to discuss the effects of integrating a spatially variable signal.

5.2.1. D″ anisotropy in global tomography models

Most global anisotropic tomography models show up to ±2% of anisotropy $\xi = (V_{SH}^2/V_{SV}^2) \leq 1.02$ in the lowermost mantle (Panning and Romanowicz, 2006; Kustowski et al., 2008; Panning et al., 2010; Chang et al., 2014; De Wit and Trampert, 2015). The exact spatial distribution of the anisotropic domain varies between models, but the transverse (SH) component of the S-velocity is dominantly faster than the radial (SV) component in domains characterized by faster than average velocities and SH is dominantly slower than SV within or in the vicinity of the LLSVPs. The present models show that SH faster than SV when averaging over a large range of propagation directions and incidence angles is only achieved for flow nearly parallel to the CMB and shear strains >2 (Figs. 3, 5, 7, 8). SH faster than SV in fast velocity domains may therefore correspond to lateral spreading of slab material at the base of the mantle. Even more constraining, although fast polarizations inclined relatively to the horizontal are produced in many models, SV faster than SH for data averaged over a large range of propagation directions and incidence angles (considering that such an average signal results from predominance of fast polarizations inclined by $>45°$ to the horizontal) is only achieved for vertical flow after significant strain, such as at the base of a downwelling (Fig. 7) or at the top of an upwelling (Fig. 8). Thus SV faster than SH are surrounded by areas with SH faster than SV, as imaged by Chang et al. (2014) in the lowermost mantle beneath the circum-Pacific subduction rim, may be consistent with transition from downwelling to shear parallel to the CMB as the slabs impact upon the CMB (Fig. 7). The measured values $\xi = (V_{SH}^2/V_{SV}^2) \leq 1.02$ are fully consistent with those predicted in the present models for simple shear parallel to the CMB Indeed, ξ, calculated by imposing to the actual elastic tensor of the aggregate a VTI symmetry (we average the tensor components over a rotation around the normal to the shear plane), is 1.03 for a shear strain of 10.

5.2.2. Sdiff and ScS waves splitting

The largest dataset investigating D″ anisotropy concerns regional studies using shear waves with grazing incidence paths. These studies have analyzed anomalies in the amplitude of the SV component of the core diffracted phase Sdiff (e.g., Vinnik et al., 1989; Lay and Young, 1991; Maupin, 1994; Cottar and Romanowicz, 2013) or performed splitting measurements on Sdiff and on S-waves reflected at the CMB (ScS), measuring the polarization anisotropy along low angle paths within D″ (e.g., Kendall and Silver, 1996; Wookey and Kendall, 2008; Nowacki et al., 2010). In the following discussion, we focus on observations in regions with higher than average velocities, possibly associated with lower temperature, in which CPO of PPv may be the dominant factor producing seismic anisotropy. Although less common, evidence for seismic anisotropy has also been reported in lowermost mantle domains with lower than average seismic velocities, like the root of the Hawaii hotspot (e.g., Fouch et al., 2001), but, in these cases, other sources for the anisotropy, such as aligned melt inclusions, should probably be invoked.

Most early studies based on Sdiff and ScS interpreted D″ anisotropy as vertically transverse isotropic (VTI). SH faster than SV was detected in D″ beneath Alaska, the Caribbean, Central and Northern Pacific, and Indian oceans. Measured delay times range from 3 to 9 s; these delay times correspond, if the anisotropy is homogeneous throughout the 1000–2800 km long paths, to birefringences of 0.5–3.0% (e.g., Kendall and Silver, 1996; Garnero and Lay, 1997; Fouch et al., 2001; Garnero and Lay, 2003). Such fast polarization data would be consistent with dominant horizontal flow in D″, but predicted delay times should be higher than those measured, unless all studies sampled by chance low birefringence propagation directions (Fig. 3). Very low anisotropy ($<0.25\%$) or isotropy was detected for a variety of NNE–NE oriented paths beneath the Central Atlantic (Garnero et al., 2004). This would imply extremely low strains in this region, since there is enough variation in the orientation of the paths to ensure that not all will sample an apparent isotropy direction. Alternate explanations for the observed apparent isotropy and/or low delay times would be the

activation of a process, like dynamic recrystallization, which would limit CPO concentration (Signorelli and Tommasi, 2015), or spatial variation in the orientation of the CPO due to changes in the flow pattern, leading to destructive interference and low integrated anisotropy along the path (or around it, since sensitivity kernels for Sdiff and ScS are wide in the lowermost mantle; Sieminski et al., 2009). We favor the second hypothesis, since recrystallization disperses, but does not randomize the CPO, and only an almost isotropic CPO would produce such low birefringence for a variety of propagation directions. The same reasoning may explain the low "average" birefringence sampled in the other studies. The NE–SW change in SH faster than SV to SV faster then SH observed in the southern Pacific (Ford et al., 2006) is consistent with a transition from flow parallel to the CMB to upwelling (Fig. 8) at the boundary of the Pacific LLSVP.

More recent studies show that: (i) the fast polarization direction of ScS waves in D″ is often inclined relative to the CMB and (ii) waves with different propagation azimuths sampling the same region in D″ display markedly different anisotropy signals. Azimuthal variations in anisotropy (both orientation of the fast polarization and delay time) and/or inclined fast S-wave polarizations were reported, for instance, below the Caribbean (Garnero et al., 2004; Maupin et al., 2005; Nowacki et al., 2010), Siberia (Wookey and Kendall, 2008), the Northern Pacific (Wookey et al., 2005), the southern edge of the African LLSVP (Cottaar and Romanowicz, 2013), and the northern edge of the Perm low S-wave anomaly beneath Russia (Long and Lynner, 2015). These results indicate that anisotropy in D″ does not have VTI symmetry, consistently with the present model predictions (Figs. 3, 5, 7, 8). They also constrain the maximum average birefringence in D″ to <2% in general, though up to 4% of birefringence is needed to explain the observations at the southern edge of the African LLSVP.

Strong variations in the intensity of the S-waves polarization anisotropy as a function of the propagation direction (back-azimuth) are predicted in all models (Figs. 3, 5, 6, 7, 8). Fast ScS polarizations inclined by >25° to the horizontal are predicted in horizontal shearing models at low shear strains (<2, Fig. 5), in 3D flow regimes in which horizontal shearing is accompanied by extension in the vertical direction (transtension, Fig. S2), and in downwelling or upwelling flows (Figs. 7 and 8). Inclined ScS fast polarizations are also observed in the horizontal segment of the downwelling corner flow streamline up to 200 km away from the change in flow direction (Fig. 7). In these domains, both the inclination of the fast polarization and the intensity of the birefringence show sharp changes as a function of the back-azimuth, with both near horizontal and inclined fast polarizations associated with either high or low birefringence.

Fast ScS polarizations inclined by 46° from the transverse direction and 4% anisotropy measured at the southern edge of the African LLSVP are consistent with the anisotropy modeled for an upwelling flow (Fig. 8), if propagation directions are at low angle to the limit of the LLSVP as in the Cottaar and Romanowicz (2013) study, since this results in sampling of the upwelling structure along a large segment of the path with propagation directions that produce fast ScS polarizations inclined by 40–50° to the horizontal. A path sampling at low angle the transition between a downwelling and shear parallel to the CMB (Fig. 7) might also explain the inclined polarizations detected beneath the northern Pacific (Wookey et al., 2005).

A spatially varying flow pattern, with paths sampling the transition between downwelling flows and shearing parallel to the CMB in different directions and positions and, hence, for different lengths (Fig. 7) might explain the changes in inclination of the fast polarization from subhorizontal to up to 45° as a function of the back-azimuth of the ScS waves beneath Siberia and the Caribbean (Wookey and Kendall, 2008; Nowacki et al., 2010).

The local birefringence predicted by the models for many propagation directions, in particular for propagation parallel to the slab strike (>4%), should nevertheless produce delay times significantly higher then those measured. As discussed in the previous section, the lower delay times measured in the seismic studies may by explained by the fact that long-period ScS waves average the anisotropy over a large volume (the anisotropic sensitivity kernels width encompasses most of the thickness of D″, Sieminski et al., 2009). Variations in the deformation pattern both along and around the path will result in a lower integrated splitting. Forward models of ScS splitting performed using both ray-theory and 3D generally-anisotropic simulations of ScS waves at the frequencies of the observations, but with no anisotropy outside the lowermost mantle show indeed that even for homogeneous anisotropy in 150 km-thick layer in D″, finite-frequency models predict delay times on average 1.5 times lower than ray-theory (Nowacki and Wookey, 2016).

5.2.3. Discrepancy between SKS and SKKS splitting

Discrepancy in splitting for SKS-SKKS records for the same earthquake-station pair has been used to probe seismic anisotropy in D″, since these waves have similar paths in the upper mantle, but different ones in D″ (piercing points of SKS and SKKS at the CMB are separated by ∼1000 km and incidence angles differ by >20°). Analysis of the modeled S-wave polarization anisotropy for horizontal simple shear (Fig. 5) shows that for shear strains >2 fast polarization directions in D″ for both SKS and SKKS are similar, being mainly close to horizontal. However, at low shear strains, for vertical flow, and in the vicinity of changes in flow direction, the fast polarization direction of SKS and SKKS waves differ by >20° for a wide range of propagation directions (Figs. 5, 7, 8). In most cases, when a discrepancy in birefringence between the two waves is present, SKKS shows a higher inclination of the fast polarization relatively to the horizontal than SKS (Figs. 5, 7, 8), but in downwelling flows, some propagation directions result in more inclined SKS fast polarizations than SKKS ones (Fig. 7). Most models also show significant variations in the intensity of the anisotropy sampled by the two waves. Thus the present models suggest that even homogeneous deformation fields might produce discordant SKS–SKKS splitting in D″. However, none of the present models produces results equivalent to the observations in the eastern Pacific, in the vicinity of the Perm anomaly, or beneath SE Asia where strong SKKS splitting with inclined fast polarizations is accompanied by almost null SKS splitting (Long, 2009; Long and Lynner, 2015; Roy et al., 2014) and very few propagation directions in a upwelling flow do result in null SKKS splitting but significant SKS splitting as also observed in the vicinity of the Perm anomaly (Long and Lynner, 2015). Such observations might be explained by changes in the flow pattern between the regions sampled by the two waves, that is at a scale <1000 km.

However, the present models bring a series of questions concerning the interpretation of SKS and SKKS data in terms of seismic anisotropy in D″. First, the models predict that SKKS and SKS should, for most flow configurations and wave propagation directions, sample significant anisotropy in D″. Yet observational evidence for such anisotropy is rare. Splitting in D″ should deviate SKS and SKKS initial polarizations from the source-receiver plane. Indeed, analysis of a large global SKS–SKKS dataset highlights the existence of such deviations, which are in general stronger for SKKS than SKS and mostly observed for waves with piercing points at CMB in higher than average velocity domains, suggesting that they may result from anisotropy in D″ due to PPv CPO, as the one modeled here (Restivo and Helffrich, 2006). Yet, this study also showed that such deviations characterize not more than 5% of the analyzed dataset and that discrepancy between SKS and SKKS splitting is even more rare. Moreover, all studies describe

a few discrepant SKS–SKKS pairs associated with a large number of coherent pairs with paths sampling nearby regions in D″ (e.g., Restivo and Helffrich, 2006; Long, 2009; Roy et al., 2014; Long and Lynner, 2015. Altogether, these observations suggest that in most cases D″ anisotropy is not effectively sampled by SKS and SKKS phases. A possible explanation may come from the consideration of finite-frequency effects. Calculation of anisotropic sensitivity kernels for SKS and SKKS shows that they have a strong sensitivity in a 50–200 km wide conic domain in the upper mantle, but a weak sensitivity distributed over a 600–1000 km wide domain in D″ (Favier and Chevrot, 2003; Sieminski et al., 2009). This implies that, even if locally the birefringence sampled by these waves is strong (up to 7–8%, Fig. 3), SKS and SKKS will only accumulate significant splitting in D″ if the anisotropy is coherent within most of this 600–1000 km wide zone. Lateral variations in flow pattern at these scales might also account for the rather low delay times measured for the discordant SKS–SKKS pairs, which imply that the maximum anisotropy levels sampled by S-waves with steeply dipping paths in D″ are <2%.

6. Conclusion

Forward models of CPO and seismic anisotropy development in a D″ layer composed by 70% of PPv and 30% of MgO based on the most recent atomic scale models of the viscoplastic deformation of these two phases predict seismic anisotropy in D″ with an orthorhombic symmetry, which produces simultaneously radial and azimuthal anisotropy components. Independently of the choice of input parameters for the PPv deformation (twinning active or not, difference in CRSS for [100] and [001] glide on the (010) plane or not), the present models indicate that the polarization of fast S-waves is often subparallel to the direction of flow in D″, but that this relation is lost at low finite strains and in the vicinity of changes in the flow pattern. The intensity of the S-waves birefringence varies strongly as a function of the propagation direction, even for a constant incidence angle relatively to the flow plane. For steady simple shear, the maximum birefringence increases from 3% at a shear strain of 1 to 6% at a shear strain of 10. Suppression of twinning in the models results in faster strenghtening of the PPv CPO with increasing strain and, hence, in higher maximum seismic anisotropies at any given finite strain.

The present models with twinning may explain most observations of seismic anisotropy in D″, in particular ScS splitting data indicating inclined (relatively to the CMB) fast polarizations, which may be produced by either vertical flows (down- or upwellings), weak horizontal shearing, transtension, or within the horizontal segment of the downwelling corner flow streamline up to 200 km away from the change in flow direction. Although the fast-polarization orientations observed using a wide variety of S-waves may be explained by simple flow patterns as the models presented here, the observed low apparent birefringence (<2%) for S-waves propagating at both low and high angle to CMB cannot be reconciled with the present model predictions (and with any CPO-induced anisotropy model, independently of the slip systems strengths used), unless finite-frequency effects and variations in the flow patterns along and around the waves paths, that is, at scales ≪1000 km, are considered. Both effects also need to be invoked to explain why only in rare cases SKS and SKKS sample significant anisotropy in D″.

Yet, in presence of spatially varying flow directions in D″ at scales below or equivalent to the path lengths in D″, which is probably the most common situation on Earth, as suggested by mantle circulation and convection models (e.g., McNamara et al., 2002; Tackley, 2011; Nowacki et al., 2013, Nowacki and Wookey, 2016), S-wave splitting measurements do not record a simple way the flow directions in D″. Forward modeling of the CPO and elastic anisotropy fields produced by different flow patterns in the mantle followed by finite-frequency calculations of the resulting seismic anisotropy seem thus an essential tool for advancing towards the ultimate goal of using seismic anisotropy data to map deformation in the deep Earth. The models presented here are a first step in this direction, as they constrain the relation between the deformation history and the evolution of elastic anisotropy of a material volume of a PPv-rich D″ layer.

Acknowledgements

We thank Ricardo Lebensohn and Carlos Tomé for making the code VPSC7c, which includes most of the last developments in viscoplastic self-consistent modeling, freely available, S. Stackhouse for assistance in defining elastic constants of ferropericlase based on Wu et al. (2013) work, S. Zhang for providing elastic constants for PPv as a function of composition, pressure, and temperature, and S. Chevrot for discussions on finite-frequency and noise effects on the measurement of seismic anisotropy in D″. Two helpful and throughout reviews are also acknowledged. Work in Lille was supported by funding from the European Research Council under the Seventh Framework Programme (FP7), ERC grant N°290424 – RheoMan.

Appendix A. Supplementary material

Supplementary material related to this article can be found online at https://doi.org/10.1016/j.epsl.2018.03.032.

References

Amodeo, J., Carrez, P., Devincre, B., Cordier, P., 2011. Multiscale modelling of MgO plasticity. Acta Mater. 59, 2291–2301.
Batchelor, G.K., 1967. An Introduction to Fluid Dynamics. Cambridge Univ. Press, New York.
Boioli, F., Carrez, P., Cordier, P., Devincre, B., Gouriet, K., Hirel, P., Kraich, A., Ritterbex, S., 2017. Pure climb creep mechanism drives flow in Earth's lower mantle. Sci. Adv. 3, e1601958.
Borgeaud, A.F., Konishi, K., Kawai, K., Geller, R.J., 2016. Finite frequency effects on apparent S-wave splitting in the D″ layer: comparison between ray theory and full-wave synthetics. Geophys. J. Int. 207, 12–28.
Bullen, K.E., 1949. Compressibility–pressure hypothesis and the Earth's interior. Mon. Not. R. Astron. Soc. 5, 355–368.
Carrez, P., Goryaeva, A., Cordier, P., 2017. Prediction of mechanical twinning in magnesium silicate post-perovskite. Sci. Rep. https://doi.org/10.1038/s41598-017-18018-1.
Chang, S.J., Ferreira, A.M., Ritsema, J., van Heijst, H.J., Woodhouse, J.H., 2014. Global radially anisotropic mantle structure from multiple datasets: a review, current challenges, and outlook. Tectonophysics 617, 1–19.
Cordier, P., Amodeo, J., Carrez, P., 2012. Modelling the rheology of MgO under Earth's mantle pressure, temperature and strain rates. Nature 481, 177–180.
Cottaar, S., Romanowicz, B., 2013. Observations of changing anisotropy across the southern margin of the African LLSVP. Geophys. J. Int. 195, 1184–1195.
De Wit, R.W.L., Trampert, J., 2015. Robust constraints on average radial lower mantle anisotropy and consequences for composition and texture. Earth Planet. Sci. Lett. 429, 101–109.
Favier, N., Chevrot, S., 2003. Sensitivity kernels for shear wave splitting in transverse isotropic media. Geophys. J. Int. 153, 213–228.
Ford, S.R., Garnero, E.J., McNamara, A., 2006. A strong lateral shear velocity gradient and anisotropy in the lowermost mantle beneath the southern Pacific. J. Geophys. Res. 111, B03306.
Fouch, M.J., Fischer, K.M., Wysession, M.E., 2001. Lowermost mantle anisotropy beneath the Pacific: imaging the source of the Hawaiian plume. Earth Planet. Sci. Lett. 190, 167–180.
Garnero, E.J., Lay, T., 1997. Lateral variations in lowermost mantle shear wave anisotropy beneath the North Pacific and Alaska. J. Geophys. Res. 102, 8121–8135.
Garnero, E.J., Lay, T., 2003. D″ shear velocity heterogeneity, anisotropy and discontinuity structure beneath the Caribbean and Central America. Phys. Earth Planet. Inter. 140, 219–242.
Garnero, E.J., Moore, M.M., Lay, T., Fouch, M.J., 2004. Isotropy or weak vertical transverse isotropy in D″ beneath the Atlantic Ocean. J. Geophys. Res. 109, B08308.
Goryaeva, A.M., Carrez, P., Cordier, P., 2015a. Modeling defects and plasticity in $MgSiO_3$ post-perovskite: Part 1—generalized stacking faults. Phys. Chem. Miner. 42, 781–792.

Goryaeva, A.M., Carrez, P., Cordier, P., 2015b. Modeling defects and plasticity in $MgSiO_3$ post-perovskite: Part 2—screw and edge [100] dislocations. Phys. Chem. Miner. 42, 793–803.
Goryaeva, A.M., Carrez, P., Cordier, P., 2016. Low viscosity and high attenuation in $MgSiO_3$ post-perovskite inferred from atomic-scale calculations. Sci. Rep. 6, 34771.
Goryaeva, A.M., Carrez, P., Cordier, P., 2017. Modeling defects and plasticity in $MgSiO_3$ post-perovskite: Part 3—screw and edge [001] dislocations. Phys. Chem. Miner. 44, 521–533.
Hirose, K., Wentzcovitch, R., Yuen, D.A., Lay, T., 2015. Mineralogy of the deep mantle – the post-perovskite phase and its geophysical significance. In: Treatise on Geophysics, pp. 85–115.
Kendall, J.M., Silver, P.G., 1996. Constraints from seismic anisotropy on the nature of the lowermost mantle. Nature 381, 409.
Komatitsch, D., Vinnik, L.P., Chevrot, S., 2010. SHdiff–SVdiff splitting in an isotropic Earth. J. Geophys. Res. 115, B07312.
Kraych, A., Carrez, P., Cordier, P., 2016. On dislocation glide in $MgSiO_3$ bridgmanite at high-pressure and high-temperature. Earth Planet. Sci. Lett. 452, 60–68.
Kustowski, B., Ekström, G., Dziewoński, A.M., 2008. Anisotropic shear-wave velocity structure of the Earth's mantle: a global model. J. Geophys. Res. 113, B06306.
Lay, T., Young, C.J., 1991. Analysis of seismic SV waves in the core's penumbra. Geophys. Res. Lett. 18, 1373–1376.
Lay, T., Williams, Q., Garnero, E.J., 1998. The core–mantle boundary layer and deep Earth dynamics. Nature 392, 461.
Lebensohn, R.A., Tomé, C.N., 1993. A self-consistent anisotropic approach for the simulation of plastic deformation and texture development of polycrystals – application to zirconium alloys. Acta Metall. Mater. 41, 2611–2624.
Lebensohn, R.A., Tomé, C.N., Ponte Castañeda, P., 2005. Improving the self-consistent predictions of texture development of polycrystals incorporating intragranular field fluctuations. Mater. Sci. Forum 495–497, 955–964.
Long, M.D., 2009. Complex anisotropy in D″ beneath the eastern Pacific from SKS–SKKS splitting discrepancies. Earth Planet. Sci. Lett. 283, 181–189.
Long, M.D., Lynner, C., 2015. Seismic anisotropy in the lowermost mantle near the Perm Anomaly. Geophys. Res. Lett. 42, 7073–7080.
Mainprice, D., Hielscher, R., Schaeben, H., 2011. Calculating anisotropic physical properties from texture data using the MTEX open source package. In: Prior, D.J., Rutter, E.H., Tatham, D.J. (Eds.), Deformation Mechanisms, Rheology and Tectonics: Microstructures, Mechanics and Anisotropy. Geol. Soc. (Lond.) Spec. Publ. 360, 175–192.
Maupin, V., 1994. On the possibility of anisotropy in the D″ layer as inferred from the polarization of diffracted S waves. Phys. Earth Planet. Inter. 87, 1–32.
Maupin, V., Garnero, E.J., Lay, T., Fouch, M.J., 2005. Azimuthal anisotropy in the D″ layer beneath the Caribbean. J. Geophys. Res. 110, B08301.
McNamara, A.K., van Keken, P.E., Karato, S.-i., 2002. Development of anisotropic structure in the Earth's lower mantle by solid-state convection. Nature 416, 310–314.
Merkel, S., McNamara, A.K., Kubo, A., Speziale, S., Miyagi, L., Meng, Y., Wenk, H.R., 2007. Deformation of (Mg, Fe) SiO_3 post-perovskite and D″ anisotropy. Science 316, 1729–1732.
Metsue, A., Carrez, Ph., Mainprice, D., Cordier, P., 2009. Numerical modeling of dislocations and deformation mechanisms in $CaIrO_3$ and $MgGeO_3$ post-perovskites – comparison with $MgSiO_3$ post-perovskite. Phys. Earth Planet. Inter. 174, 165–173.
Miyagi, L., Nishiyama, N., Wang, Y., Kubo, A., West, D.V., Cava, R.J., Duff, T.S., Wenk, H.R., 2008. Deformation and texture development in $CaIrO_3$ post-perovskite phase up to 6 GPa and 1300 K. Earth Planet. Sci. Lett. 268, 515–525.
Miyagi, L., Kanitpanyacharoen, W., Kaercher, P., Lee, K.K., Wenk, H.R., 2010. Slip systems in MgSiO3 post-perovskite: implications for D″ anisotropy. Science 329, 1639–1641.
Molinari, A., Canova, G.R., Ahzi, S., 1987. A self-consistent approach of the large deformation polycrystal viscoplasticity. Acta Metall. 35, 2983–2994.
Monteiller, V., Chevrot, S., 2010. How to make robust splitting measurements for single-station analysis and three-dimensional imaging of seismic anisotropy. Geophys. J. Int. 182, 311–328.
Niwa, K., Miyajima, N., Seto, Y., Ohgushi, K., Gotou, H., Yagi, T., 2012. Insitu observation of shear stress-induced perovskite to post-perovskite phase transition in $CaIrO_3$ and the development of its deformation texture in a diamond-anvil cell up to 30 GPa. Phys. Earth Planet. Inter. 194, 10–17.
Nowacki, A., Wookey, J., Kendall, J.M., 2010. Deformation of the lowermost mantle from seismic anisotropy. Nature 467, 1091–1094.
Nowacki, A., Walker, A.M., Wookey, J., Kendall, J.M., 2013. Evaluating post-perovskite as a cause of D″ anisotropy in regions of paleosubduction. Geophys. J. Int. 192, 1085–1090.
Nowacki, A., Wookey, J., 2016. The limits of ray theory when measuring shear wave splitting in the lowermost mantle with ScS waves. Geophys. J. Int. 207, 1573–1583.
Panning, M., Romanowicz, B., 2006. Three-dimensional radially anisotropic model of shear velocity in the whole mantle. Geophys. J. Int. 167, 361–379.
Panning, M.P., Lekić, V., Romanowicz, B.A., 2010. Importance of crustal corrections in the development of a new global model of radial anisotropy. J. Geophys. Res. 115, B12325.
Reali, R., Boioli, F., Gouriet, K., Carrez, P., Devincre, B., Cordier, P., 2017. Modeling plasticity of MgO by 2.5 D dislocation dynamics simulations. Mater. Sci. Eng. A 690, 52–61.
Restivo, A., Helffrich, G., 2006. Core–mantle boundary structure investigated using SKS and SKKS polarization anomalies. Geophys. J. Int. 165, 288–302.
Roy, S.K., Kumar, R., Srinagesh, D., 2014. Upper and lower mantle anisotropy inferred from comprehensive SKS and SKKS splitting measurements from India. Earth Planet. Sci. Lett. 392, 192–206.
Sieminski, A., Trampert, J., Tromp, J., 2009. Principal component analysis of anisotropic finite-frequency kernels. Geophys. J. Int. 179, 1186–1198.
Signorelli, J., Tommasi, A., 2015. Modeling the effect of subgrain rotation recrystallization on the evolution of olivine crystal preferred orientations in simple shear. Earth Planet. Sci. Lett. 430, 356–366.
Tackley, P., 2011. Living dead slabs in 3-D: the dynamics of compositionally-stratified slabs entering a "slab graveyar D″ above the core–mantle boundary. Phys. Earth Planet. Inter. 188, 150–162.
Thomas, C., Kendall, J.-M., 2002. The lowermost mantle beneath northern Asia—II. Evidence for lower-mantle anisotropy. Geophys. J. Int. 151, 296–308.
Thomas, C., Wookey, J., Brodholt, J., Fieseler, T., 2011. Anisotropy as cause for polarity reversals of D″ reflections. Earth Planet. Sci. Lett. 307, 369–376.
Thurel, E., Cordier, P., 2003. Plastic deformation of wadsleyite: I. High-pressure deformation in compression. Phys. Chem. Miner. 30, 256–266.
Tomé, C.N., Lebensohn, R.A., Kocks, U.F., 1991. A model for texture development dominated by deformation twinning: application to zirconium alloys. Acta Metall. Mater. 39, 2667.
van der Hilst, R.D., de Hoop, M.V., Wang, P., Shim, S.-H., Ma, P., Tenorio, L., 2007. Earth's core–mantle boundary region seismostratigraphy and thermal structure. Science 315, 813–816.
Vinnik, L.P., Farra, V., Romanowicz, B., 1989. Observational evidence for diffracted SV in the shadow of the Earth's core. Geophys. Res. Lett. 16, 519–522.
Walker, A.M., Forte, A.M., Wookey, J., Nowacki, A., Kendall, J.-M., 2011. Elastic anisotropy of D″ predicted from global models of mantle flow. Geochem. Geophys. Geosyst. 12, 1–22.
Walker, A.M., Dobson, D.P., Wookey, J., Nowacki, A., Forte, A.M., 2017. The anisotropic signal of topotaxy during phase transitions in D″. Phys. Earth Planet. Inter. 276, 159–171.
Wenk, H.-R., Speziale, S., McNamara, A.K., Garnero, E.J., 2006. Modeling lower mantle anisotropy development in a subducting slab. Earth Planet. Sci. Lett. 245, 302–314.
Wenk, H.-R., Armann, M., Burlini, L., Kunze, K., Bortolotti, M., 2009. Large strain shearing of halite: experimental and theoretical evidence for dynamic texture changes. Earth Planet. Sci. Lett. 280, 205–210.
Wenk, H.-R., Cottaar, S., Tomé, C.N., McNamara, A., Romanowicz, B., 2011. Deformation in the lowermost mantle: from polycrystal plasticity to seismic anisotropy. Earth Planet. Sci. Lett. 306, 33–45.
Wookey, J., Kendall, J.M., Rümpker, G., 2005. Lowermost mantle anisotropy beneath the North Pacific from differential S-ScS splitting. Geophys. J. Int. 161, 829–838.
Wookey, J., Kendall, J.M., 2008. Constraints on lowermost mantle mineralogy and fabric beneath Siberia from seismic anisotropy. Earth Planet. Sci. Lett. 275, 32–42.
Wu, Z., Justo, J.F., Wentzcovitch, R.M., 2013. Elastic anomalies in a spin-crossover system: ferropericlase at lower mantle conditions. Phys. Rev. Lett. 110, 228501.
Wu, X., Lin, J.F., Kaercher, P., Mao, Z., Liu, J., Wenk, H.R., Prakapenka, V.B., 2017. Seismic anisotropy of the D″ layer induced by (001) deformation of post-perovskite. Nat. Commun. 8, 14669.
Yamazaki, D., Yoshino, T., Ohfuji, H., Ando, J.I., Yoneda, A., 2006. Origin of seismic anisotropy in the D″ layer inferred from shear deformation experiments on post-perovskite phase. Earth Planet. Sci. Lett. 252, 372–378.
Zhang, S., Cottaar, S., Liu, T., Stackhouse, S., Militzer, B., 2016. High-pressure, temperature elasticity of Fe- and Al-bearing $MgSiO_3$: implications for the Earths lower mantle. Earth Planet. Sci. Lett. 434, 264–273.